RMetS
Royal Meteorological Society

A numerical study of rotating convection during tropical cyclogenesis

Gerard Kilroy and Roger K. Smith*
Meteorological Institute, Ludwig Maximilians University of Munich, Germany

*Correspondence to: Roger K. Smith, Meteorological Institute, Ludwig Maximilians University of Munich, Theresienstr. 37, 80333 Munich, Germany. E-mail: roger.smith@lmu.de

We present idealized numerical model experiments to investigate the convective generation of vertical vorticity in a tropical depression. The ambient vertical vorticity is represented by a uniform solid-body rotation. The calculations are motivated by observations made during the Pre-Depression Investigation of Cloud-systems in the Tropics (PREDICT) experiment. A specific aim is to isolate and quantify the effects of low- to mid-level dry air on convective cells that form within a depression and, in particular, on the generation of vertical vorticity in these cells. The results do not support a common perception that dry air aloft produces stronger convective downdraughts and more intense, cold-air outflows therefrom. Indeed, we find that dry air aloft weakens both updraughts and downdraughts, corroborating the recent results of James and Markowski.

As in the recent calculations of Wissmeier and Smith, the growing convective cells locally amplify the ambient rotation at low levels by more than an order of magnitude and this vorticity, which is produced by the stretching of existing ambient vorticity, persists long after the initial updraught has decayed. Moreover, significant amplification of vorticity occurs even for clouds of only moderate vertical extent. The maximum amplification of vorticity is relatively insensitive to the maximum updraught strength, or the height at which it occurs, and it is not unduly affected by the presence of dry air aloft. Thus the presence of dry air is not detrimental to the amplification of low-level vorticity, although it reduces the depth through which ambient vorticity is enhanced.

Results for a limited number of different environmental soundings indicate that the maximum amplification of vorticity increases monotonically with the strength of the thermal perturbation that initiates the convection, but the amount of increase depends also on the thermodynamic structure of the sounding.

Key Words: vortical hot towers; dry air; moist convection

Received 8 March 2012; Revised 5 July 2012; Accepted 9 July 2012; Published online in Wiley Online Library 11 October 2012

Citation: Kilroy G, Smith RK. 2013. A numerical study of rotating convection during tropical cyclogenesis. *Q. J. R. Meteorol. Soc.* **139**: 1255–1269. DOI:10.1002/qj.2022

1. Introduction

The PREDICT experiment was carried out during the period 15 August–30 September 2010 to gather data on tropical depressions with the ultimate aim of better understanding the processes that lead to tropical cyclogenesis.* A specific aim was to test the so-called 'marsupial paradigm' for

*A recent review of tropical cyclogenesis is given by Montgomery and Smith (2011).

cyclogenesis proposed in a recent theoretical article by Dunkerton *et al.* (2009). This paradigm rests on the idea that the synoptic-scale wave in which a large proportion of Atlantic, Caribbean and Eastern Pacific hurricanes form contains a protected region, or 'pouch', consisting of a closed cyclonic circulation in the low to middle troposphere in a frame of reference moving with the wave. The pouch region has weak deformation and provides a set of closed material contours inside which air is repeatedly moistened by convection, being protected from the lateral intrusion of dry air and deformation by horizontal or vertical shear.

The experiment was based in St Croix in the US Virgin Islands and its central facility was the National Centre for Atmospheric Research GV research aircraft, a twin-engined jet that has a typical flight duration of 9 h and can fly at altitudes of up to about 14 km. The aircraft was used to release Global Positioning System (GPS) dropsondes to measure the vertical structure of wind and thermodynamic quantities in tropical disturbances. A total of 26 missions were flown, sampling eight tropical disturbances. Further details and some early results of the experiment are presented by Montgomery *et al.* (2012). The present study was motivated by observations of one particular disturbance that was declared Tropical Storm *Gaston* on 1 September 2010 by the National Hurricane Center, but which was downgraded on 2 September to a tropical depression after data from the first PREDICT mission into the disturbance became available. The disturbance maintained an identity that could be tracked across the Caribbean although the convective activity weakened considerably after 7 September. Five GV flights were made into the disturbance on each day from 2–7 September, excepting 4 September.

During the weather briefings for the experiment, there was much speculation that the storm failed to redevelop because of its weak pouch that enabled dry air to penetrate its core. The presumption was that the dry air in the lower to middle troposphere would strengthen downdraughts from deep convection and flood the boundary layer with low-entropy air from above. However, later analyses of the dropwindsonde data showed that the mission average low-level pseudo-equivalent potential temperature increased during the five days during which the storm was monitored (Smith and Montgomery, 2012). While some of this increase may have been due to the increase in sea-surface temperature as the disturbance tracked westwards, there is certainly no evidence of a reduction on a day-to-day time-scale that might have thwarted *Gaston*'s redevelopment. The question then is: Are there other aspects of the convection that might be influenced by the presence of dry air that might ultimately be detrimental to cyclogenesis?

Numerical model simulations show that when convection occurs in an environment of non-zero vertical vorticity, updraughts amplify the vorticity by the process of vortex-tube stretching (Hendricks *et al.*, 2004; Saunders and Montgomery, 2004; Montgomery *et al.*, 2006; Rozoff, 2007; Nguyen *et al.*, 2008; Wissmeier and Smith, 2011). Using a cloud model, Wissmeier and Smith (2011) showed that even moderately deep clouds can produce a large amplification (by one to two orders of magnitude) of the vertical component of absolute vorticity on time-scales of an hour, even for a background rotation rate typical of the undisturbed tropical atmosphere. The vorticity so produced has a maximum in the lower troposphere and persists long after the initial updraught has decayed. They showed also that the tangential wind speeds induced by a single updraught are typically no more than a few metres per second with a horizontal scale of the order of a kilometre and would be barely detectable by normal measurement methods in the presence of an ambient wind field. Their results suggest that all tropical convection away from the equator is vortical to some degree and can significantly amplify the vertical vorticity locally. It is not hard to imagine, then, that the stretching of vertical vortex tubes by a developing cumulus cloud is a fundamental process and that it may be an important process in tropical cyclogenesis. In fact, vortical convective clouds have been identified as fundamental building blocks during both tropical cyclone genesis and the intensification process (Hendricks *et al.*, 2004; Montgomery *et al.*, 2006; Nguyen *et al.*, 2008; Braun *et al.*, 2010; Fang and Zhang, 2010).

The foregoing studies indicate that like-signed vortical remnants generated by convective clouds tend to aggregate in a quasi-two-dimensional manner with a corresponding upscale energy cascade and some of these remnants are intensified further by subsequent convective episodes. If the disturbance-scale circulation strengthens, the vorticity remnants tend to become axisymmetrized by the associated angular shear flow. In addition, system-scale inflow forced by the aggregate latent heating from convective elements leads to an inward advection of convectively enhanced vorticity. Stokes' theorem applied to a fixed area *surrounding the convection* implies that there will be an accompanying increase in strength of the disturbance-scale circulation on account of the import[†] of ambient absolute vorticity into it. When applied to a fixed area *within the convective region*, the import of convectively enhanced vorticity into the area will lead also to an increase in the circulation. As the circulation progressively increases in strength, there is some increase in the surface moisture fluxes. However, it is not necessary that the moisture fluxes continue to increase with surface wind speed (Montgomery *et al.*, 2009). This research forms the basis of a unified view of tropical cyclogenesis and intensification (Montgomery and Smith, 2011). In this view, the separate stages proposed in previous significant studies and reviews (e.g. Frank, 1987; Emanuel, 1989; McBride, 1995; Karyampudi and Pierce, 2002; Tory and Frank, 2010) are unnecessary.

Over the years, the common perception that dry air generally enhances the strength of convective downdraughts has been challenged in one way or another by a number of authors (Brown and Zhang, 1997; Tompkins, 2001; Redelsperger *et al.*, 2002; Sobel *et al.*, 2004; Kuchera and Parker, 2006; Rozoff, 2007; Holloway and Neelin, 2009; James and Markowski, 2009; Minoru and Sugiyama, 2010). For example, James and Markowski (2009) performed numerical experiments to determine the effects of dry air aloft on quasi-linear convective systems. Using idealized soundings of differing values of Convective Available Potential Energy (CAPE) and moisture content, they found that dry air aloft exerts detrimental effects on overall convective intensity, weakening both updraughts and downdraughts. They found also that in an environment

[†]The stretching and thereby amplification of ambient (or system-scale) vorticity by convection by itself does not lead to an increase in the circulation around a fixed loop embedded in the flow because stretching leads to a contraction in the areal extent of the amplified vorticity (see Haynes and McIntyre, 1987).

with large CAPE, the influence of dry air is minimized. They attributed the reason for weakened convection to a decline in hydrometeor mixing ratios, as updraught buoyancy is diluted by dry air entrainment and also downdraught strength is weakened by smaller rates of ice melting. However, they did find that for cloud environments with high CAPE, dry air strengthened mesoscale downdraughts in regions of stratiform precipitation. Kuchera and Parker (2006) found also that dry mid-level air is not uniquely associated with strong downdraughts leading to damaging gust fronts.

The above findings motivate the question: if *convective* downdraughts are not strengthened by the presence of dry air, what aspects of the ensuing convection might be detrimental to tropical cyclogenesis? Is it simply the fact that mesoscale downdraughts are strengthened, or is it that, by reducing the updraught strength, the dry air reduces the ability of the convection to amplify vorticity? It is the latter question that is a focus of the present study. The study extends that of Wissmeier and Smith (2011), with the specific aim of quantifying the effects of dry air aloft on deep convection in a tropical depression environment and, in particular, on the ability of the convection to amplify ambient rotation. It is conceivable that a reduction of the ability of the convection to amplify ambient rotation might have a more detrimental effect on tropical cyclogenesis than the effects of downdraughts by reducing the propensity of deep convective cells to aggregate. As a necessary first step, we focus here on the effects of dry air on a single-cloud updraught using thermodynamic soundings based on the data for ex-*Gaston*. We examine also the dependence of the ensuing convection on the temperature excess of the initial bubble. A study of the more complex questions concerning the subsequent cloud merger is currently underway.

The article is organized as follows. In section 2 we give a brief description of the numerical model and the configuration of the experiments. The results are presented in section 3 and the conclusions in section 4.

2. The numerical model

Following Wissmeier and Smith (2011), the numerical model used for this study is the state-of-the-art three-dimensional cloud model of Bryan and Fritsch (2002) and Bryan (2002), the same model that was used also by James and Markowski (2009). It is important to note that the model retains several terms in the governing thermodynamic and pressure equations that are often neglected in atmospheric models; in particular the model accounts for the heat content of hydrometeors (Bryan and Fritsch, 2002). The model incorporates a parametrization scheme for warm rain processes as well as one for processes involving ice microphysics. The latter is Gilmore's Li-scheme, in which cloud water, rain water, cloud ice, snow and hail/graupel are predicted (Gilmore *et al.*, 2004). The model has no parametrization of the planetary boundary layer. For simplicity, radiation effects are neglected and there are no surface fluxes of momentum, heat and moisture. A sixth-order horizontal advection scheme, which is not diffusive, is chosen. An additional artificial filter is applied for stability. A suitable coefficient for this diffusion was suggested by George Bryan (personal correspondence). This scheme is applied to all variables.

2.1. Model configuration

The experiments use the same model configurations as that of Experiment 9 from Wissmeier and Smith (2011), except that the horizontal domain size and grid spacing are halved to give improved horizontal resolution of the cloud updraughts. The horizontal domain size is 25 km × 25 km with a uniform horizontal grid spacing of 250 m. The vertical domain extends to a height of 25 km with the vertical grid interval stretching smoothly from 120 m at the surface to 1000 m at the top. There are 47 grid levels in the vertical, eight of which are below 850 mb. The large time step is 3.7 s and the integration time is 2 h. There are eight small time steps per large time step to resolve fast-moving sound waves. The default 'open' boundary conditions are used at the lateral boundaries. A sponge layer is implemented in the uppermost 2 km to inhibit the reflection of gravity waves from the upper boundary. All experiments include both warm rain processes and the ice microphysics scheme.

2.2. Initiation of convection

Convection is initiated in a quiescent environment by a symmetric thermal perturbation with a horizontal radius of 5 km and a vertical extent of 1 km. The temperature excess has a maximum at the surface at the centre of the perturbation and decreases monotonically to zero at the perturbation's edge. The perturbation centre coincides with the centre of the domain. In general, the details of the ensuing convection such as the maximum updraught strength and the updraught depth will depend on the spatial structure and amplitude of the thermal perturbation. While this method for the initiation of convection is necessarily artificial, it is unclear how to significantly improve upon it and for this reason it has been widely used in numerical studies of deep convection (see e.g. Weisman and Klemp, 1982; Gilmore *et al.*, 2004; Rozoff, 2007; Wissmeier, 2009[‡]) and by Wissmeier and Smith (2011). Table 1 shows the temperature perturbation used in the various experiments described here.

In reality, thermal perturbations over the ocean will be linked to surface heat fluxes, but there are other ways in which convection may be triggered such as lifting at gust-front boundaries generated by prior convection. For this reason, other methods for storm initiation have been used in previous studies. One method is to begin with a low-level cold pool that induces sufficient lifting at its boundary to bring environmental air to its level of free convection (LFC: e.g. Trier *et al.*, 1996; Wissmeier *et al.*, 2010; Fierro *et al.*, 2012). Another method is simply to impose a vertical velocity at low levels to achieve the same result (e.g. Ferrier and Houze, 1989). Both methods are unsuitable for implementation in the simple thought experiments formulated here, where the desire is to initiate an updraught that is axisymmetric.

2.3. Representation of vertical vorticity

The calculations are carried out on an f-plane with the Coriolis parameter $f = \zeta_0$, where $\zeta_0 = 1.5 \times 10^{-4}\ \mathrm{s}^{-1}$. This

[‡]Section 3.4.2 therein examines the sensitivity of the storm's initial updraught strength on the warm bubble parameters (width, depth, temperature excess).

value is typical of the vertical vorticity at low levels in ex-Tropical Storm *Gaston* (Mark Boothe, personal communication). The use of an f-plane with an enhanced value of f beyond a typical tropical value is a simple expedient to model the background rotation of the vortex in the present problem. For further simplicity, we have omitted both horizontal and vertical wind shear in representing the pouch environment. One of our main goals is to examine and quantify the amplification of the background rotation by deep convection in such an environment, starting with an initial uniform background rotation and an environmental sounding. The choice of soundings is discussed in section 2.4.

2.4. *Numerical experiments*

The distinguishing features of the ten numerical experiments discussed in this article are the environmental sounding used and the maximum temperature excess of the thermal perturbation that initiates the updraught. The soundings examined are a small subset of those obtained from dropsondes launched during the missions into ex-*Gaston* on 2, 3 and 5 September, 2010, but span a reasonable range of sounding types in the pouch region. As soundings were limited to the ceiling of the aircraft (about 14 km), they were extended vertically using analysis data in their proximity from the European Centre for Medium Range Weather Forecasts 0.25° analyses. A list of all soundings used is presented in Table 1. The table lists also the relevant parameters of these experiments, including the thermodynamic characteristics of the soundings, their date and time and the initial temperature perturbation used to initiate convection.

2.4.1. *Experiments with idealized soundings*

The first three experiments are designed to explore the role of moisture on the dynamics and thermodynamics of the ensuing updraught and downdraught. Experiment 1 uses an idealized sounding with piecewise-linear profiles of virtual potential temperature, θ_v, and mixing ratio, r. This sounding approximates that obtained from the dropsonde launched at 1820 UTC on 5 September into ex-Tropical Storm *Gaston*, but has somewhat lower CAPE (2770 J kg^{-1} compared with 3500 J kg^{-1}). The observed sounding was made near the centre of the low-level circulation in a region of high total precipitable water (TPW), high CAPE[§] and zero convective inhibition (CIN).[¶] In fact, it had the largest TPW, 65.2 kg m^{-2}, on that day.

Experiment 1 serves as a control for comparison with Experiments 2 and 3, which have decreasing amounts of mid-level moisture. Experiment 2 has the same moisture

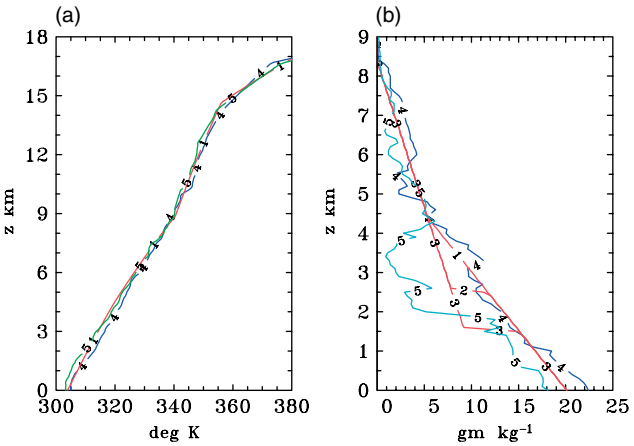

Figure 1. Three idealized soundings used for Experiments 1–3 and two actual soundings from ex-Tropical Storm *Gaston* on 5 September obtained during the PREDICT Experiment. Shown are virtual potential temperature on the left and mixing ratio on the right. Sounding labelled '1' is the control (Experiment 1), while those labelled '2' and '3' are modified versions thereof, giving a progressively drier atmosphere at mid-levels (but with the same virtual potential temperature to preserve the CAPE and CIN). The sounding labelled '4' refers to the profile with the highest moisture content in ex-*Gaston* on 5 September (TPW = 65.2 kg m^{-2}), while that labelled '5' is one of the driest profiles observed on that day (TPW = 43.5 kg m^{-2}). This figure is available in colour online at wileyonlinelibrary.com/journal/qj

profile as that of Experiment 1 from the surface to 2.5 km and above 4.5 km. In the layer between these heights, the mixing ratio is reduced by extending the linear profile of mixing ratio at upper levels down to 2.5 km, as shown in Figure 1(b). The relative humidity for the 'dry' region between 2.5 km and 4.5 km is an average of 66%, compared with 83% for Experiment 1. Experiment 3 is similar to Experiment 2, but the upper-level mixing ratio profile is reduced down to 1.5 km as shown in Figure 1(b). The relative humidity for the 'dry' region is then 63% compared with 83% for the control. The reduced moisture lowers the TPW values to 59.3 kg m^{-2} for Experiment 2 and 54.8 kg m^{-2} for Experiment 3. The temperature profile of both altered soundings is adjusted slightly to preserve the virtual temperature of the control sounding, ensuring that each sounding has identical CAPE. Experiments based on these soundings are used to investigate the sensitivity of the cloud updraught and downdraught to dry air aloft.

2.4.2. *Experiments with observed soundings*

Experiment 4 is carried out with the observed sounding on which Experiment 1 was based while, Experiment 5 is carried out with the sounding at 1448 UTC, which is one of the driest on that day with a TPW of 43.5 kg m^{-2} (see Figure 2 of Smith and Montgomery (2012)). Again, the flow environment is taken to be quiescent. It is seen that the idealized profiles are broadly realistic: the θ_v profiles of all soundings are very similar (Figure 1(a)) and the mixing ratios in Experiments 1–3 lie within those of the driest and moistest soundings made on 5 September (Figure 1(b)). The two observed soundings are illustrated by the curves labelled '4' and '5' in Figure 1. The sounding in Experiment 5 has a CAPE value of 1145 J kg^{-1}, only a third of that in Experiment 4, and a CIN of 21 J kg^{-1}. Five additional experiments were carried out using other observed profiles, three to examine the dependence of the ensuing convection on the temperature excess of the initial bubble for a sounding of moderate

[§]We remind the reader that CAPE is a parcel quantity that typically has a strong negative vertical gradient in the lower troposphere. For this reason, the values cited herein are based on an average for air parcels lifted from the surface and at 100 m intervals above the surface to a height of 500 m. Since the calculation of CAPE is a nonlinear function of temperature and moisture, we prefer this method to one based on averaged values of temperature and mixing ratio through a surface-based layer of air with some arbitrarily prescribed depth.

[¶]Like CAPE, CIN is a quantity that also refers to an air parcel. Rather than computing an average up to 500 m as for CAPE, it seems physically more reasonable to examine the minimum value of of CIN up to this level.

Table 1. Launch time and details of the ten experiments studied herein. CAPE averaged from the surface to 500 m in J kg^{-1}, minimum CIN between the surface and 500 m in J kg^{-1}, and total precipitable water (TPW) in kg m^{-2}. ΔT refers to the strength of the initial thermal perturbation. * refers to an idealized profile created using dropsonde data from the given date and time as a basis.

Exp #	Sounding Date d/m/yy	Sounding Time UTC	TPW kg m^{-2}	CAPE J kg^{-1}	CIN J kg^{-1}	ΔT K
1	5/9/10*	18:20	62.3	2770	40	2
2	5/9/10*	18:20	59.3	2770	40	2
3	5/9/10*	18:20	54.8	2770	40	2
4	5/9/10	18:20	65.2	3500	0	2
5	5/9/10	14:48	43.5	1145	21	2
6	2/9/10	17:03	67.1	1650	0	2
7	2/9/10	17:03	67.1	1650	0	1
8	2/9/10	17:03	67.1	1650	0	0.25
9	3/9/10	17:57	58.7	1900	5	2
10	3/9/10	17:57	58.7	1900	5	3.5

CAPE (1650 J kg^{-1}) and zero CIN, for soundings where the parcel buoyancy is expected to be relatively large at low altitudes (Experiments 6–8), and two soundings with a moderate CAPE (1900 J kg^{-1}) and small CIN (5 J kg^{-1}) to examine the structure of convection where the parcel buoyancy is expected to become appreciable only above 2 km (Experiments 9–10). Further details of these experiments are given in the relevant subsections.

3. Results

3.1. Convective cell evolution

Much of our interest herein is focussed on the life cycle of the first convective updraught triggered by the initial thermal bubble, i.e. the first hour of the simulation. The evolution of the updraught is summarized by time–height cross-sections of various quantities at the centre of the domain, where the initial updraught forms. Figure 2 shows cross-sections of vertical velocity w and density temperature difference $\mathrm{d}T_\rho$ between the updraught and the environment for Experiments 1–3, respectively. The quantity $\mathrm{d}T_\rho$ is a measure of the buoyancy including the effects of water loading (Emanuel, 1994, chapter 2). Figure 3 shows cross-sections of total liquid water (cloud water plus rainwater) and total ice content (hail, graupel, snow and ice) for these experiments. Table 2 gives details of the updraught and downdraught strength for all experiments. These details include the maximum density temperature difference between the updraught and the environment ($\mathrm{d}T_{\rho\,\max}$), the maximum liquid water content ($q_{L\max}$), the maximum ice content ($q_{\mathrm{Ice\,max}}$), the maximum density temperature difference ($\mathrm{d}T_{\rho\,\min}$) between the downdraught and the environment and the maximum difference in pseudo-equivalent potential temperature ($\mathrm{d}\theta_{\mathrm{e\,min}}$) between the downdraught and the environment at the surface.

In all ten experiments, the flow evolution is similar to that described many times previously (see Wissmeier and Smith, 2011, section 4.1). In brief, the updraught that forms the first convective cell is initiated by the buoyancy of the initial bubble. The updraught develops slowly at first, but increases rapidly in vertical extent and strength as additional buoyancy is generated by the latent heat released by condensation. Cloud water produced by condensation is carried aloft in the updraught, and if it ascends high enough it freezes, thereby generating additional buoyancy through the latent heat of fusion. A fraction of the condensate grows large enough to fall against the updraught as ice, snow or rain and subsequently generates a downdraught.

Figure 4 shows vertical cross-sections of selected fields through the domain centre in Experiment 1 at 30 min, when the initial cloud is still growing rapidly, and at 60 min, when the updraught has decayed. Panel (a) shows isopleths of the vertical mass flux $M = \rho_o(x,z)w(x,z)$ with the 0.2 g kg^{-1} contour of cloud water plus ice and the 0.5 g kg^{-1} contour of rain water superimposed at 30 min. At this time, the mass flux is generally positive throughout the cloud, but there is a narrow strip of subsidence around the upper part of the cloud as the cloud penetrates the air above it.

Figure 4(b) shows the corresponding cross-section of $\mathrm{d}T_\rho$. The positive values through much of the cloud indicate that the updraught is still buoyant through much of its depth, despite the water loading. There is a region of negative buoyancy below 2 km, which is in part a result of water loading and in part due to the lifting of stably stratified air below the updraught following the ascent of the warm bubble initiating convection (note that this negative buoyancy extends laterally well beyond the region of water loading). The two areas of positive buoyancy on either side of the cloud are associated with transient subsidence as the updraught penetrates the stably stratified environmental air and the area of negative buoyancy near the cloud top is associated with the forced ascent of stably stratified environmental air ahead of the cloud. This time is just prior to that when ice begins to form.

Figure 4(c) shows the cross-section of pseudo-equivalent potential temperature, θ_e, at 30 min and illustrates how the cloud is effectively a plume of relatively high near-surface values of θ_e that mixes with lower values of θ_e from low and middle tropospheric levels as it ascends.

The cross-section of the vertical component of relative vorticity, ζ, at 30 min indicates that there is a significant amplification of the ambient vorticity extending almost to the top of the cloud, but the vorticity generated is a maximum at low levels (Figure 4(d)). These findings corroborate those of Wissmeier and Smith (2011). This amplification of vorticity is a result of the stretching of ambient absolute vorticity by the vertical gradient of the mass flux, which is positive at this time up to a height of a little over 6 km (Figure 4(a)). The evolution of ζ will be examined in more detail in section 3.3.

While the assumption of an axisymmetric thermal rising in an environment without vertical shear is certainly an idealization, it is not totally unrealistic as suggested by the

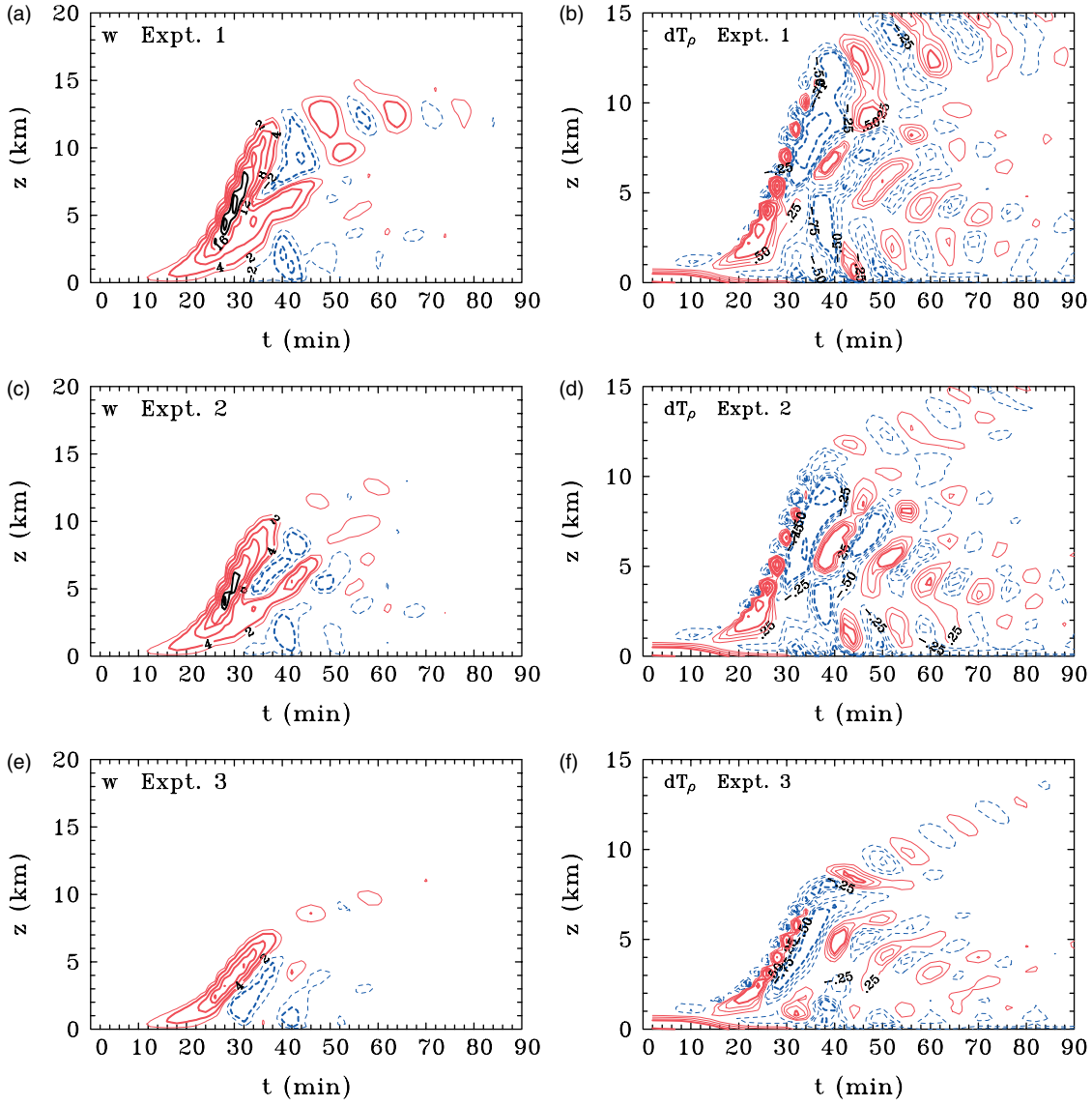

Figure 2. Height–time series of maximum vertical velocity w (left column) and density temperature difference between the updraught and its environment dT_ρ (right column) taken at the centre of the updraught in Experiments 1–3. Contour interval for w: thin contours 2 m s^{-1}, thick contours 4 m s^{-1}. Thick black contours show values above 20 m s^{-1} and are in intervals of 5 m s^{-1}. Solid contours (red in the online article) show positive values, dashed contours (blue in the online article) negative values. Contour interval for dT_ρ: thin contours 0.25 K, 0.5 K, 0.75 K, thick contours 1 K. This figure is available in colour online at wileyonlinelibrary.com/journal/qj

Table 2. Maximum vertical velocity (w_{max}) at the centre of the domain, the height of this maximum ($z(w_{max})$), minimum vertical velocity below 10 km (w_{min}) at the centre of the domain, the height of this minimum ($z(w_{min})$), the maximum liquid water content ($q_{L\ max}$) and the maximum ice content ($q_{Ice\ max}$) in Experiments 1–10. Also listed are the density perturbation temperature ($dT_{\rho\ max}$), the height of this maximum, the minimum surface density perturbation temperature ($dT_{\rho\ min}$), which indicates the strength of the low-level cold pool, and the minimum surface pseudo-equivalent potential temperature depression ($d\theta_{e\ min}$).

Expt.	w_{max} m s^{-1}	$z(w_{max})$ km	w_{min} m s^{-1}	$z(w_{min})$ km	$q_{L\ max}$ g kg^{-1}	$q_{Ice\ max}$ g kg^{-1}	$dT_{\rho\ max}$ K	$z(dT_{\rho\ max})$ km	$dT_{\rho\ min}$ K	$d\theta_{e\ min}$ K
1	27.1	6.5	−9.6	1.3	11.4	8.6	4.4	4.0	−2.6	−21.0
2	25.0	4.7	−7.6	2.5	10.1	7.1	4.1	3.8	−1.9	−15.4
3	16.5	2.8	−6.9	2.2	6.4	2.2	2.4	3.2	−0.8	−20.2
4	34.0	10.5	−10.9	6.1	16.7	16.6	8.2	8.4	−3.8	−10.0
5	11.4	3.1	−6.3	1.6	6.1	0.3	2.0	1.0	−2.3	−0.5
6	34.0	12.0	−6.0	3.5	15.1	10.1	4.6	11.8	−3.7	−13.2
7	28.0	11.7	−6.0	3.1	14.4	8.1	3.4	4.4	−4.5	−11.4
8	21.0	13.1	−5.3	2.5	12.0	5.5	3.1	4.2	−3.9	−12.4
9	27.7	7.6	−9.9	3.1	9.7	9.1	5.2	5.8	−3.7	−3.3
10	27.7	6.5	−11.4	2.2	13.8	12.2	6.0	6.6	−3.4	−17.5

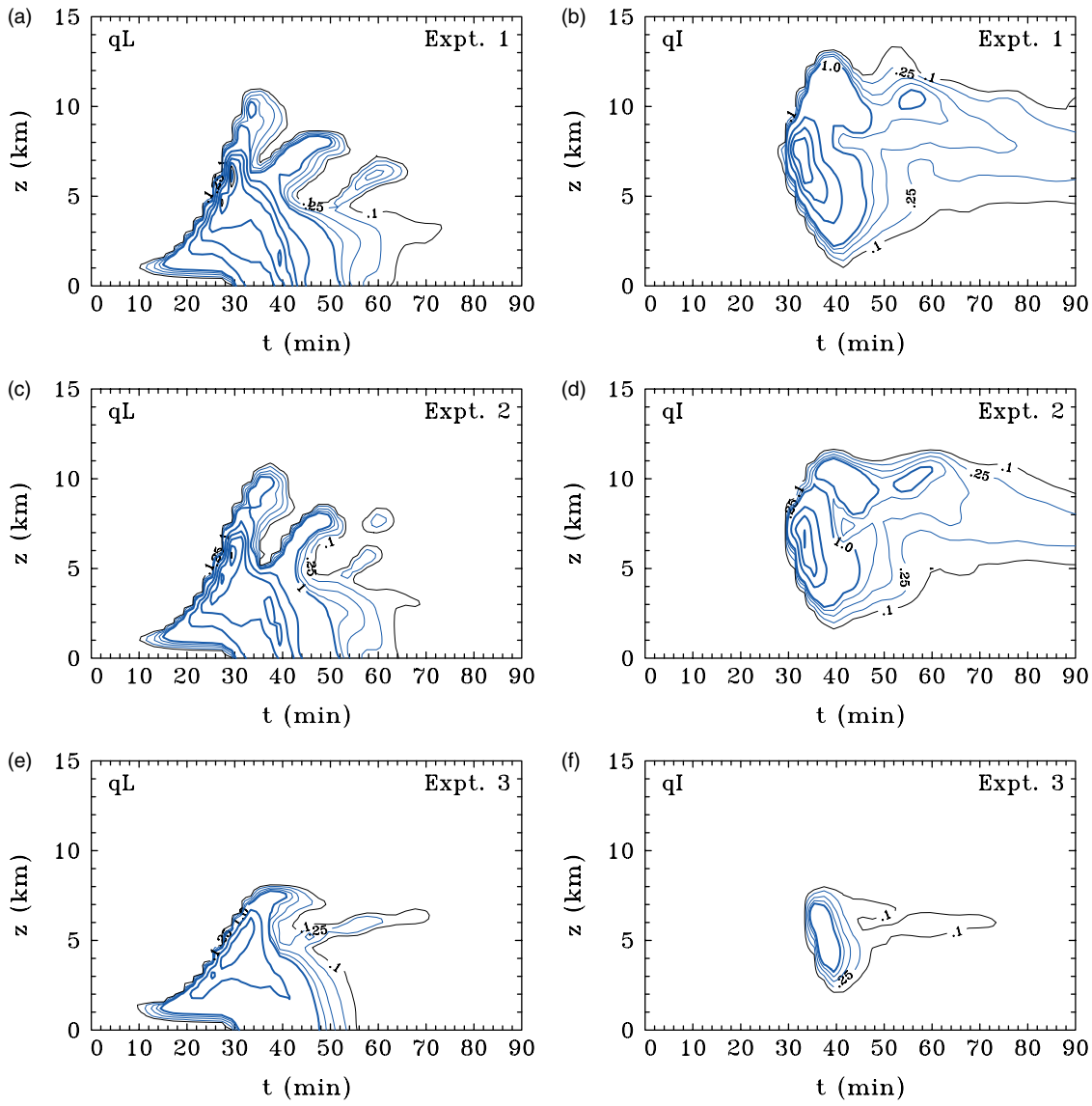

Figure 3. Height–time series of maximum total liquid water (cloud water + rain water) taken at the centre of the updraught (left panels) and maximum total ice water (snow, ice, hail and graupel; right panels) in Experiments 1–3. Contour interval: thin contours 0.1, 0.25, 0.5 and 0.75 g kg^{-1}; thick contours 2 g kg^{-1} starting at 1 g kg^{-1}. This figure is available in colour online at wileyonlinelibrary.com/journal/qj

cloud in the photograph of a moderately deep, precipitating cumulus congestus cloud shown in Figure 5.

The updraught in Experiment 1 attains a maximum value of 27.1 m s^{-1} at a height of 6.5 km after about 26 minutes (see Figure 2(a) and Table 2). The updraught subsequently decays because of mixing with ambient air and water loading. The water loading initiates a downdraught that is cooled as a result of melting and sublimation. The cooling is aided by the partial evaporation of rain as it falls into unsaturated air below cloud base. Finally, a pool of cold air forms and spreads out near the surface.

The lower panels of Figure 4 show similar vertical cross-sections to the upper panels, but at 60 min. At this time, the updraught has all but decayed (panel (e)), but a plume of enhanced relative vorticity remains within and below the cloud (panel (h)). The amplified vorticity is a legacy of that generated by stretching during the earlier stages of updraught development. There is little remaining positive buoyancy in the cloud, which is mostly composed of an anvil of ice and a decaying rain shaft that has negative buoyancy (panel (f)). There is a marked layer of cool downdraught air at the surface. The θ_e cross-section at this time (panel (g)) shows that the plume generated by the updraught has been replaced by one generated by the downdraught, which has brought air with low values of θ_e near to the surface. Of interest is how these structures are modified by the presence of dry air aloft, a topic that we examine in the next subsection.

Secondary cells of convection may be triggered along the cold pool's spreading gust front if the air ahead of it is sufficiently unstable. This happens in Experiments 4 and 6–8. In these, the subsequent flow evolution becomes more complicated than that shown in Figure 4, losing its axisymmetric structure.

At this point it is worth drawing attention to the likeness between the time–height cross-sections shown in Figures 2–4 and those of Ferrier and Houze (1989; their figures 7, 8 and 10) obtained using a one-dimensional cloud model. Since we do not have to make many of the assumptions that they did, our results may be interpreted as support for the realism of their simple model.

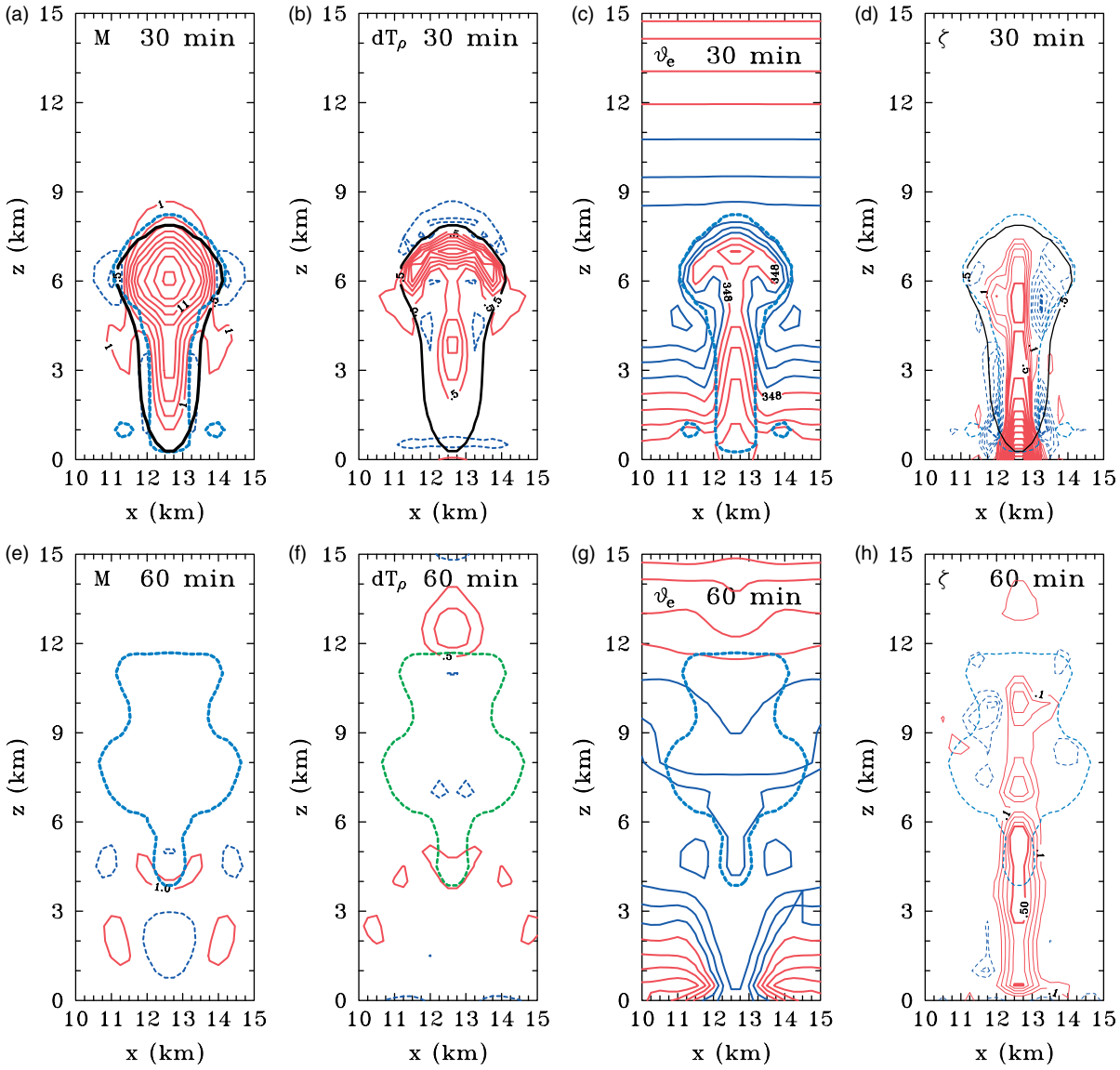

Figure 4. Vertical cross-sections through the domain centre of (a, e) vertical mass flux M, (b, f) density temperature difference dT_ρ between the cloud and its environment, (c, g) pseudo-equivalent potential temperature θ_e, and (d, h) the vertical component of relative vorticity ζ in Experiment 1 at 30 min (upper row) and 60 min (lower row). Also shown are the cloud boundaries, characterized by the 0.1 g kg^{-1} contour of cloud water + ice (light blue thick dashed curve) and the rain shaft, characterized by the 0.5 g kg^{-1} contour of rain water (thick black curve). In panel (f), the region of ice is delineated by the 0.1 g kg^{-1} contour of ice (green thick dashed curve). The calculations using a square horizontal grid lead to a weak azimuthal wavenumber-4 asymmetry that is most prominent in the vorticity field. This asymmetry accounts for the departures from axisymmetric features in panels (d) and (h). Contour interval: for M, 1 kg s^{-1} m^{-2}; for dT_ρ, 0.5 K; for θ_e, 3 K; for ζ, thin contours 5×10^{-4} s^{-1}. Contours of θ_e change colour from blue at 345 K to red at and above 348 K.

3.2. *The effects of dry air aloft*

A comparison the values of w_{max} for Experiments 1, 2 and 3 in Table 2 shows that updraught is significantly weakened in Experiment 3 when moisture is removed from the lowest levels (i.e. below 2.5 km), but less so when these levels remain moist (Experiment 2). The updraughts in Experiments 2 and 3 have maximum values of 25 m s^{-1} and 16.5 m s^{-1} at heights of 4.7 and 2.8 km, respectively. Thus the presence of the environmental layer of dry air reduces the updraught strength as well as the altitude attained by the updraught, the reduction being most dramatic in Experiment 3. The foregoing reductions are a manifestation of the diminished updraught buoyancy (compare panels (b), (d) and (f) in Figure 2). Note that the maximum buoyancy in Experiment 1 is nearly double that of Experiment 3 ($dT_{\rho\ max}$ = 2.4 K compared with 4.4 K). As expected, there is a monotonic relationship between the maximum vertical velocity and the maximum buoyancy.

The reduced buoyancy may be attributed to the entrainment of the drier air, which decreases the amount of water that condenses and therefore the amount of latent heat release. The effect is evident in a comparison of the liquid water and ice mixing ratios between the three experiments (see Figure 3 and Table 2). The maximum liquid water content is 10.1 g kg^{-1} in Experiment 2 and only 6.4 g kg^{-1} in Experiment 3, compared with 11.4 g kg^{-1} in Experiment 1. The lower liquid water content means also that there are fewer water particles to freeze and therefore less generation of additional buoyancy above the freezing level by the latent heat of freezing. Note that in Experiment 1, a relatively large ice mixing ratio leads to a large vertical velocity maximum at a height of 6.5 km. In contrast, there are comparatively few ice hydrometeors in Experiment 3 as the cloud ascends

Figure 5. Photograph of a precipitating cumulus congestus cloud with little or no vertical shear in the lower and middle the troposphere taken from the Pacific Island of Guam in August 2008. This figure is available in colour online at wileyonlinelibrary.com/journal/qj

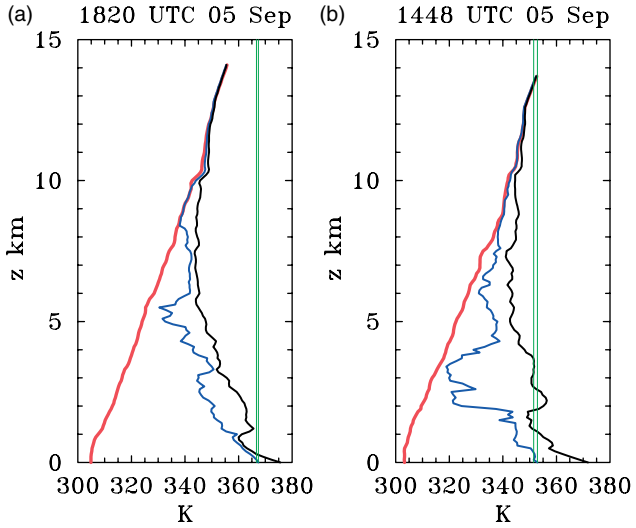

Figure 6. Vertical profiles of θ_v, θ_e and θ_{es} for two soundings made in ex-*Gaston* on 5 September: (left) 1820 UTC and (right) 1448 UTC. The left curves (red in the online article) show θ_v, the middle curves (blue in the online article) show θ_e and the right curves (black) saturated θ_{es}. The locations of these soundings relative to the TPW and surface pressure distribution are shown in Figure 1 of Smith and Montgomery (2012). The vertical lines in the figure show the θ_e values for air parcels at the surface and at a height of 100 m above the surface. This figure is available in colour online at wileyonlinelibrary.com/journal/qj

only slightly above the freezing level, which is about 5.5 km high.

The foregoing results are supported by those of Experiments 4 and 5. These use observed soundings of temperature and humidity with similar profiles of θ_v to the idealized profile in Experiments 1–3, but have differing amounts of low-level moisture (Figure 1). Additional information about these soundings is contained in Figure 6, which compares the vertical structure of θ_v, θ_e[‖] and saturation pseudo-equivalent potential temperature (θ_{es}) for each of them. The former sounding lies in the region of highest TPW near the centre of circulation and the latter in the drier air to the south of this region (the location of the soundings in relation to the TPW and surface pressure distributions are shown in Figure 2 of Smith and Montgomery, 2012).

The vertical lines in Figure 6 show the θ_e values for air parcels at the surface and at a height of 100 m above the surface. Since θ_e is conserved[**] for undilute ascent with or without condensation, these lines represent the θ_e of moist air parcels lifted from these levels. Moreover, the distance between the vertical line and the θ_{es} curve at a given height is roughly proportional to the buoyancy of the lifted air parcel at this height, with the buoyancy being positive when the parcel line is to the right of the θ_{es} curve. Thus, assuming undilute ascent, the first intersection of the vertical line with the θ_{es} curve is the approximate LFC and the final intersection is approximately equal to the level of neutral buoyancy (LNB) for the particular air parcel (see Ooyama, 1969; Emanuel, 1994; Holton, 2004). Furthermore, the area between these lines and the θ_{es} curve in the range between the LFC and LNB is roughly proportional to the CAPE and that between the surface and the LFC is roughly proportional to the CIN.

Time–height cross-sections of vertical velocity for Experiments 4 and 5 are shown in Figure 7. The maximum updraught and downdraught velocities in Experiment 4 are 34 and 10.9 m s^{-1}, respectively (see Figure 7(a) and Table 2). These values are both larger than the corresponding values in Experiment 1, which are 27.1 and 9.6 m s^{-1}, respectively. The maximum buoyancy, characterized by $\mathrm{d}T_{\rho\ \max}$, is larger also (8.2 K compared with 4.4 K). These differences may be attributed to the fact that the mixing ratio is 1–2 g kg^{-1} larger in Experiment 4 below a height of 1 km (Figure 1). In contrast, the maximum updraught velocity in Experiment 5 (11.4 m s^{-1}) is less than that in Experiment 3 (16.5 m s^{-1}), also the maximum buoyancy is slightly weaker (2 K compared with 2.4 K). Further, the updraught only just extends above the freezing level so that there is little ice produced and little latent heat of fusion released. The downdraught velocity is only marginally less than that in Experiment 3 (6.3 m s^{-1} compared with 6.9 m s^{-1}). These differences are presumably because the sounding in Experiment 5 is drier than that in Experiment 3 in the air layer between about 2 and 4 km and near the surface (see Figure 1(b)).

At this point it is worth noting that the maximum vertical velocities in Experiments 1, 2 and 4, which range between 25 and 34 m s^{-1}, are somewhat high compared with those commonly reported in deep tropical convection, where values in the range 10–25 m s^{-1} are more typical (LeMone and Zipser, 1980; Houze *et al.*, 2009). The high values here, which were only on the axis, are presumably due to the strength of the thermal bubble (2 K), which may be unrealistically large for thermal perturbations over the tropical oceans. When we repeated Experiments 1–3 with a 1.5 K bubble, the maximum vertical velocities were reduced to 22.5, 18.7 and 8.6 m s^{-1}, but all the conclusions regarding the effects of dry air discussed below were unchanged. However, when these experiments were repeated with a 1 K bubble, convection was not initiated in any of them. We chose a 2 K bubble so that deep convection would be initiated in all experiments. Finally, it is worth noting also that the maximum observed vertical velocities determined by aircraft penetrations may be expected to have a bias

[‖]The pseudo-equivalent potential temperature was calculated using Bolton's formula (Bolton, 1980).
[**]It is perhaps worth noting that the numerical model used here only conserves θ_e approximately.

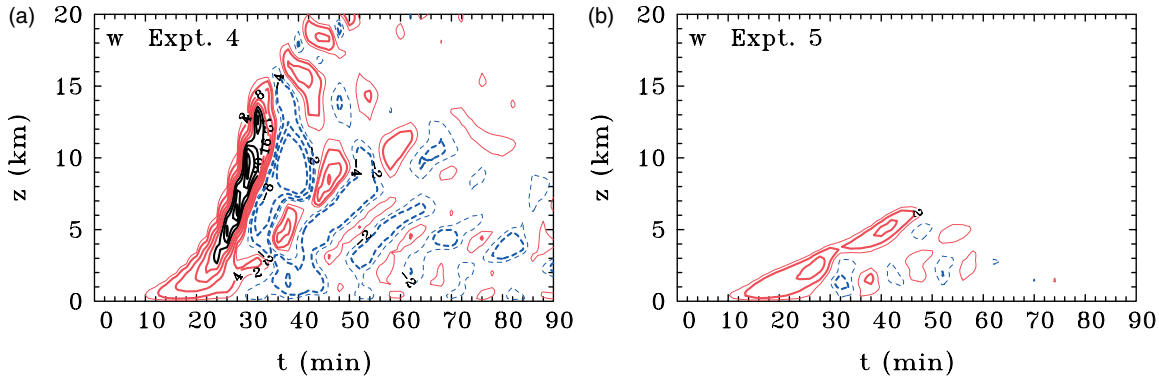

Figure 7. Height–time series of maximum vertical velocity w at the centre of the updraught in (a) Experiment 4 and (b) Experiment 5. Contour interval for w: thin contours 2 m s^{-1}, thick contours 4 m s^{-1}. Thick black contours show values above 20 m s^{-1} and are in intervals of 5 m s^{-1}. Solid contours (red in the online article) show positive values, dashed contours (blue in the online article) negative values. This figure is available in colour online at wileyonlinelibrary.com/journal/qj

because, for safety reasons, pilots will not normally fly into the most intense updraughts.

Traditional reasoning would suggest that the ensuing convection within a relatively dry mid-level environment would lead to comparatively strong downdraughts (e.g. Emanuel, 1994). However, this idea is not borne out by the results of the present calculations. Indeed, in Experiments 1–3 the strongest downdraught (9.6 m s^{-1}) occurs in Experiment 1, while the downdraughts become progressively weaker as the environment becomes drier (see Table 2). The negative buoyancy of the downdraught characterized by $\mathrm{d}T_{\rho\ \mathrm{min}}$ diminishes also with increasing dryness, being −2.6 K in Experiment 1, −1.9 K in Experiment 2 and only −0.8 K in Experiment 3.

In the drier environment of Experiments 2 and 3, the negative vertical gradient of θ_e is much larger at low levels than in Experiment 1, especially just above 1 km, where the dry air is introduced (see Figure 1(b)). Thus, the weaker downdraughts in Experiment 3 are able to bring down low-θ_e air into the boundary layer with θ_e values comparable to those in Experiment 1 (note that $\mathrm{d}\theta_{e\ \mathrm{min}}$ is −21 K in Experiment 1 and −20.2 K in Experiment 3: see Table 2). For this reason, the minimum depression in θ_e does not decrease monotonically in Experiments 1–3 and, perhaps not surprisingly, there is not a monotonic relationship between $\mathrm{d}\theta_{e\ \mathrm{min}}$ and $\mathrm{d}T_{\rho\ \mathrm{min}}$ in Table 2.

A similar finding concerning the dependence of downdraught strength on mid-level dryness was described in a recent numerical modelling study of mid-latitude convective systems (both quasi-linear systems and supercells) by James and Markowski (2009). They found that dry air aloft 'reduces the intensity of the convection, as measured by updraft mass flux and total condensation and rainfall. In high-CAPE line-type simulations, the downdraught mass flux and cold pool strength were enhanced at the rear of the trailing stratiform region in a drier environment. However, the downdraft and cold pool strengths were unchanged in the convective region, and were also unchanged or reduced in simulations of supercells and of line-type systems at lower CAPE.' They noted also that 'when dry air was present, the decline in hydrometeor mass exerted a negative tendency on the diabatic cooling rates and acted to offset the favourable effects of dry air for cooling by evaporation. Thus, with the exception of the rearward portions of the high-CAPE line-type simulations, dry air was unable to strengthen the downdrafts and cold pool.' Weaker downdraughts would be

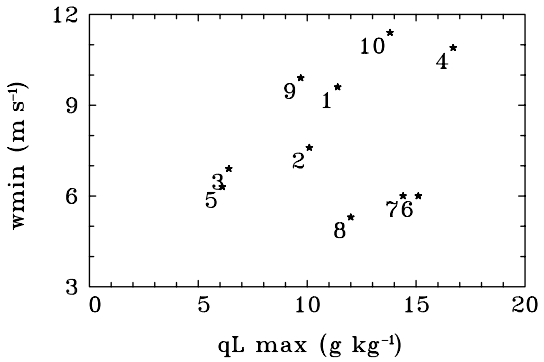

Figure 8. Scatter plot of maximum downdraught velocity against maximum liquid water content (marked by star symbols) in Experiments 1–10 (indicated by the numbers).

expected if the water loading, characterized by the sum of liquid water and ice mixing ratios, is decreased. The presence of fewer ice hydrometeors would lead to less cooling due to melting and sublimation and fewer raindrops would lead also to less cooling by partial evaporation below cloud base. These features are confirmed by the experiments carried out here. As seen in Table 2 and in the scatter plot of Figure 8, the experiments with lower liquid water content in a particular set (Experiments 1–5, 9–10)[††] have weaker downdraughts. In fact, a drier environment leads to weaker updraughts and downdraughts irrespective of the presence of ice hydrometeors. This result was demonstrated by repeating Experiments 1–3 with the ice microphysics scheme switched off (not shown).

It was thought by PREDICT forecasters that the failure of ex-Tropical Storm *Gaston* to redevelop was because dry Saharan air layer aloft suppressed the system by flooding the boundary layer with cool downdraught air. The dry air was evident in multiple satellite products. The Saharan air layer is considered hostile to Atlantic tropical convection (Dunion and Veldon, 2004). Our experiments with dry air aloft suggest an alternative hypothesis for the failure of ex-Tropical Storm *Gaston* to redevelop. By weakening the updraught strength, the dry air would make the updraught less effective in amplifying vertical vorticity. We examine this effect in the next section.

[††] Experiments 6–10 are discussed later in this section.

3.3. The amplification of ambient vertical vorticity

Since the pioneering study of Hendricks *et al.* (2004), there is growing evidence that all deep convection, and even convection of moderate vertical extent, produces a significant amplification of existing local vertical vorticity by vortex-tube stretching, even in the absence of ambient vertical shear (Wissmeier and Smith, 2011, and references). There is evidence also that this convectively generated vorticity is important in both the genesis of tropical cyclones (e.g. Hendricks *et al.*, 2004; Montgomery *et al.*, 2006) and their intensification (e.g. Nguyen *et al.*, 2008; Shin and Smith, 2008; Fang and Zhang, 2010). Such vorticity is able to interact with like-signed patches of vorticity produced by neighbouring convective cells, to be strengthened further by subsequent convection and to be progressively axisymmetrized by the angular shear of the parent vortex as discussed in Montgomery *et al.* (2006) and Nguyen *et al.* (2008). These findings naturally motivate the question foreshadowed in the Introduction: if the most important effect of mid-level dry air on convective clouds is to reduce the updraught strength rather than to increase the downdraught strength, is the detrimental effect of dry air on tropical cyclogenesis simply that it reduces the ability of the convection to amplify locally the ambient vertical vorticity? While an answer to this question calls for model simulations in which there are many clouds, it is still pertinent to quantify the effects of dry air on the ability of a single cloud to amplify vorticity.

Wissmeier and Smith (2011) showed that the first updraught produces a large amplification of the background vorticity at low levels and that this vorticity remains after the updraught has decayed. The same occurs in the calculations carried out here as seen in the vertical cross-sections of ζ shown in Figure 4, in the time–height cross-sections of vertical vorticity for Experiments 1–8 shown in Figure 9 and in the values for the maximum vertical vorticity ($\zeta_{\max}$) as a fraction of the background vorticity (ζ_1) in Table 3. The maxima of $\zeta_{\max}/\zeta_1$ in Table 3 and the time of their occurrence, $t_{\zeta_{\max}}$, refer to the first convective updraught, which, as noted earlier, forms along the axis. The third and and fourth column of the table list the maximum values of ζ attained *in any location* and their times of occurrence. This is because, in Experiments 4 and 6–8, new updraughts are triggered along the gust front produced by the initial cell and these amplify the existing vertical vorticity further.

The maximum amplification by the first updraught in Experiments 1–3 is about 85–88 times the background vorticity and occurs at the surface after about 24 min. Perhaps surprisingly, the magnitude of the amplification is insensitive to the maximum updraught strength or vertical extent of the cloud, although deeper clouds produce an amplification of the vorticity through a deeper layer of the atmosphere (cf. panels (a), (b) and (c) of Figure 9). An even larger amplification occurs in Experiments 4 and 5 (117 times in the former and 121 times in the latter) despite the large difference in the vertical extent of the updraughts in these two experiments (see Figure 2).

The fact that $\zeta_{\max}/\zeta_1$ is virtually the same in Experiments 1–3, which all have the same temperature and moisture profiles below a height of 1.5 km, suggests that factors other than the sounding play a role in determining the amplification of vorticity. One possible factor is the strength of the inital thermal perturbation, since this quantity determines the vertical profile of buoyancy and its time variation. In turn, the buoyancy profile determines the vertical gradient of the vertical mass flux that is responsible for the production of vertical vorticity by the stretching of existing vorticity. The similarities between $\zeta_{\max}/\zeta_1$ in Experiments 4 and 5 would then be attributable to the fact that there are only slight differences between the temperature and moisture profiles at low levels in these experiments. Further investigation of the effects of the strength of the initial thermal bubble is the topic of the next section.

Table 3. The degree of amplification of the ambient vorticity by the first updraught cell ($\zeta_{\max}/\zeta_1$) and the time ($t_{\zeta_{\max}}$) at which it occurs, and the degree of amplification of the ambient vorticity over the entire domain ($\zeta_{\mathrm{dom-max}}/\zeta_1$) to capture further amplification by secondary cells, should they occur. Also listed is the time of this secondary maximum, $t_{\zeta_{\mathrm{dom-max}}}$.

A blank value indicates that secondary convection was not triggered.

Expt.	$\zeta_{\max}/\zeta_1$	$t_{\zeta_{\max}}$ min	$\zeta_{\mathrm{dom-max}}/\zeta_1$	$t_{\zeta_{\mathrm{dom-max}}}$ min
1	88	26	–	–
2	88	26	–	–
3	85	24	–	–
4	117	28	197	82
5	121	40	–	–
6	122	28	173	54
7	94	30	180	72
8	48	42	170	96
9	121	28	–	–
10	139	24	–	–

3.4. Sensitivity to initial bubble strength

The three Experiments 6–8 all use the sounding made in ex-Tropical Storm *Gaston* at 1703 UTC on 2 September (see left panel of Figure 10), but have initial thermal bubbles with temperature excesses of 2, 1 and 0.25 K respectively. The sounding has a lower value of CAPE than that in Experiment 4 (1650 J kg^{-1} compared with 3500 J kg^{-1}), but a slightly larger TPW (67.1 kg m^{-2} compared with 65.2 kg m^{-2}). Moreover, like Experiment 4 it has zero CIN (see section 2.4.1 for the definition of CIN used here). Thus convection is easily initiated, even with an initial thermal perturbation of 0.25 K. These three experiments are designed to assess the role played by the strength of the initial bubble on the ensuing convection.

The evolution of the updraught in the three experiments is shown in Figure 11 and a comparison of maximum updraught strengths is detailed in Table 2. As expected, a decrease in strength of the initial thermal perturbation leads to a monotonic decrease in the maximum updraught strength, the maximum liquid water and ice contents and the maximum density perturbation temperature. However, the downdraught strength does not change appreciably (it varies by less than 1 m s^{-1}). Even so, in the case with the initial thermal perturbation of only 0.25 K, convection reaches a depth of 15 km. The maximum amplification of vertical vorticity in the three experiments is 122, 94 and 48 times, respectively, i.e. it decreases monotonically with the temperature excess of the initial bubble, in line with the arguments given in the previous section.

As noted above, new updraughts are triggered along the gust front produced by the initial cell in Experiments 4 and 6–8 (note that these experiments have soundings

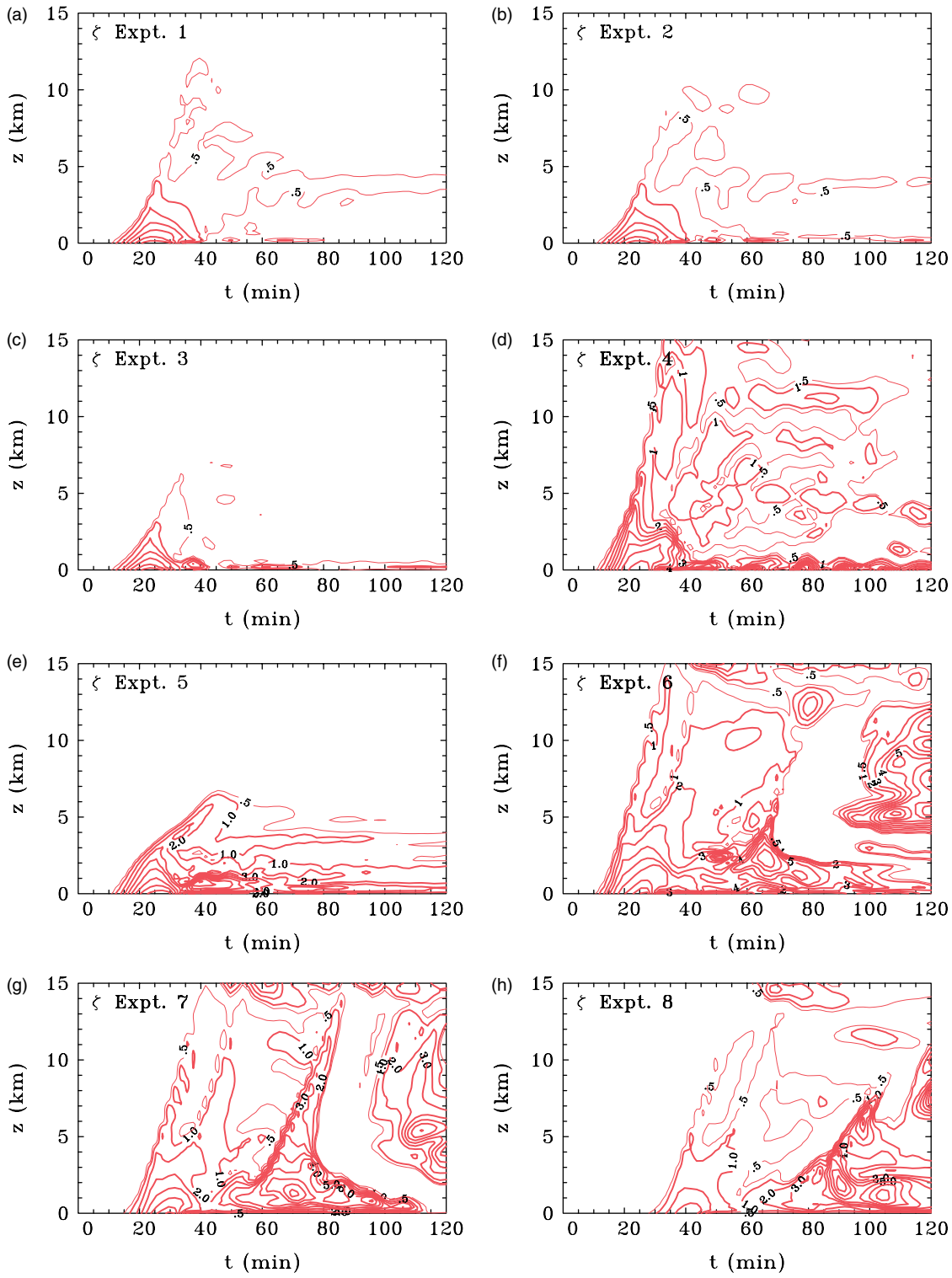

Figure 9. Height–time cross-sections of maximum vertical component of relative vorticity taken in the centre of the updraught in Experiments 1–8. Contour interval = 1×10^{-3} s^{-1}. Solid contours (red in the online article) show positive values, dashed contours (blue in the online article) negative values. The thin solid curve shows the 0.5×10^{-3} s^{-1} contour. This figure is available in colour online at wileyonlinelibrary.com/journal/qj

with zero CIN: see Table 1). These updraughts amplify the existing vertical vorticity further as indicated in the two right columns of Table 3. The amplification of relative vorticity in Experiment 4 increases from 117 times the background ambient value after the first cell to 197 times in subsequent cells. Similar increases are found in Experiments 6–8. In particular, the amplification by secondary cells in Experiment 8 is 170 times the background ambient value, which is over three times the amplification produced by the initial cell. The evolution of the maximum relative vorticity for Experiments 6–8 is shown in Figure 11(d).

Experiments 9 and 10 use the sounding made in ex-Tropical Storm *Gaston* at 1757 UTC on 3 September (see right panel of Figure 10), which is typical of those on the periphery of the pouch and has a lower CAPE than in Experiments 6–8 and non-zero CIN (see Table 2). Experiment 9 is initialized with a 2 K thermal perturbation and in this case the initial updraught produces a 121×

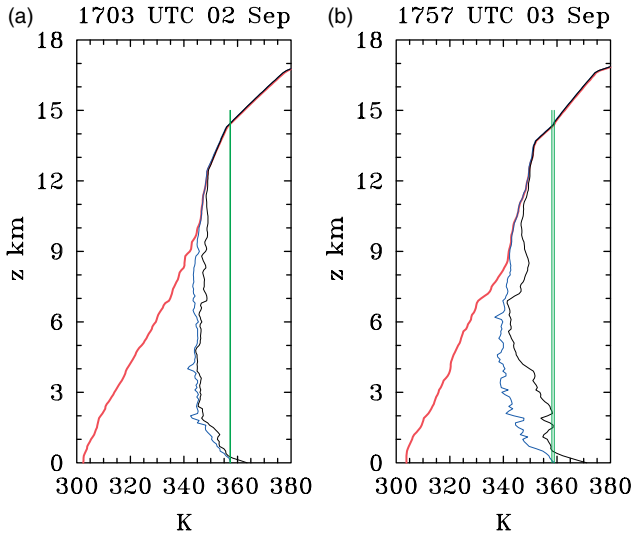

Figure 10. Legend as for Figure 6, but for the two soundings in ex-*Gaston* at (left) 1703 UTC on 2 September and (right) 1757 UTC on 3 September. This figure is available in colour online at wileyonlinelibrary.com/journal/qj

amplification of the vorticity. In contrast, in Experiment 10, which is initialized with a 3.5 K thermal perturbation, the first updraught cell produces a 139× amplification of the vorticity. As in the previous experiments, there is a monotonic increase in the maximum amplification of vorticity with increasing strength of the thermal perturbation.

3.5. *Relevance to tropical cyclogenesis*

The precise way in which the stretching and thereby amplification of ambient vertical vorticity in clouds impacts tropical cyclogenesis remains a topic of active research. However, a range of numerical simulations to date (e.g. by Hendricks *et al.*, 2004; Montgomery *et al.*, 2006; Nguyen *et al.*, 2008; Shin and Smith, 2008; Fang and Zhang, 2010) indicate that the amplification of vertical vorticity by clouds is followed by a merger, aggregation and subsequent axisymmetrization of the remnant vorticity anomalies, leading to an upscale cascade of cyclonic vorticity to form a nascent vortex. The aggregation process is assisted by the system-scale convergence driven by the collective buoyancy of the clouds themselves. In the presence of ambient vertical shear, the clouds generate anticyclonic vorticity anomalies also by tilting horizontal vortex tubes into the vertical, but the cyclonic anomalies tend to be stronger as a result of the existing cyclonic ambient vorticity. Nevertheless, a segregation mechanism comes into play in which like-signed vorticity anomalies agglomerate, with the stronger cyclonic anomalies ultimately becoming the dominant features. As discussed in the foregoing articles (see e.g. Nguyen *et al.*, 2008, section 3.1.5), the merger and segregation processes can be understood broadly in terms of barotropic dynamics, although the finer details of these processes in a baroclinic vortex are still under investigation.

In the context of the foregoing remarks, we draw attention to a recent article by Braun *et al.* (2012), which investigates the impact of dry mid-level air on tropical-cyclone intensification (not genesis) using idealized model simulations. The study investigates the potential negative influence of dry mid-level air on intensification, in particular 'its role in enhancing cold downdraft activity and suppressing storm development'. Specifically, they use the Weather Research and Forecasting model to construct two sets of idealized simulations of tropical-cyclone development in environments with different configurations of dry air. A principal finding is that 'dry air slows the intensification only when it is located very close to the vortex core at early times', but that 'all storms eventually reached the same steady-state intensity'. The study appears to be built on the premise that mid-level dry air should enhance cold downdraft activity, but a finding was that '... strong downdraft cooling in and of itself does not necessarily inhibit intensification. Instead, it may need to be coupled with the production of storm asymmetries that have the potential to dramatically change the radial distribution of diabatic heating and push the heating peak away from the high vorticity core.' Interestingly, no mention is made about the possible effects of dry air on the generation of in-cloud vertical vorticity, which the studies referenced in the paragraph above have shown to be a prominent feature of the tropical-cyclone intensification process.

4. Conclusions

We have described a series of numerical experiments designed to isolate the effects of dry air aloft on deep convection, including the efficacy of the convection in amplifying the vertical component of low-level ambient vorticity. Experiments were carried out also to determine the effects of the initial thermal trigger on the ensuing convection. The main focus was on convection that develops within a tropical depression environment using a few thermodynamic soundings acquired during the 2010 PREDICT experiment, or idealized soundings based on these. The initial structure of vertical vorticity was idealized by assuming solid-body rotation, but with a value characteristic of disturbances observed during the experiment.

The calculations do not support a common perception that dry air aloft produces stronger convective downdraughts and more intense outflows. Rather, the entrainment of dry air aloft was found to weaken both convective updraughts and downdraughts. Consistent with the recent findings of Wissmeier and Smith (2011), growing convective cells locally amplify the ambient rotation at low levels by more than an order of magnitude and this vorticity, which is produced by the stretching of existing ambient vorticity, persists long after the initial updraught has decayed.

Significant amplification of vorticity occurs even for clouds of only moderate vertical extent. The maximum amplification of vorticity is relatively insensitive to the maximum updraught strength and/or the height at which it occurs. Extending the findings of Wissmeier and Smith (2011), we showed that the degree of amplification is insensitive to the presence of dry air aloft. Thus our results provide an answer to the question posed earlier: does the reduction of the updraught strength by dry-air entrainment have the most detrimental effect on tropical cyclogenesis by reducing the ability of the convection to amplify ambient rotation? Our results suggest that the answer to this question is no. Nevertheless, the reduction in the depth of the strengthened rotation may be an important effect of dry air on the dynamics of tropical cyclogenesis. For example, we

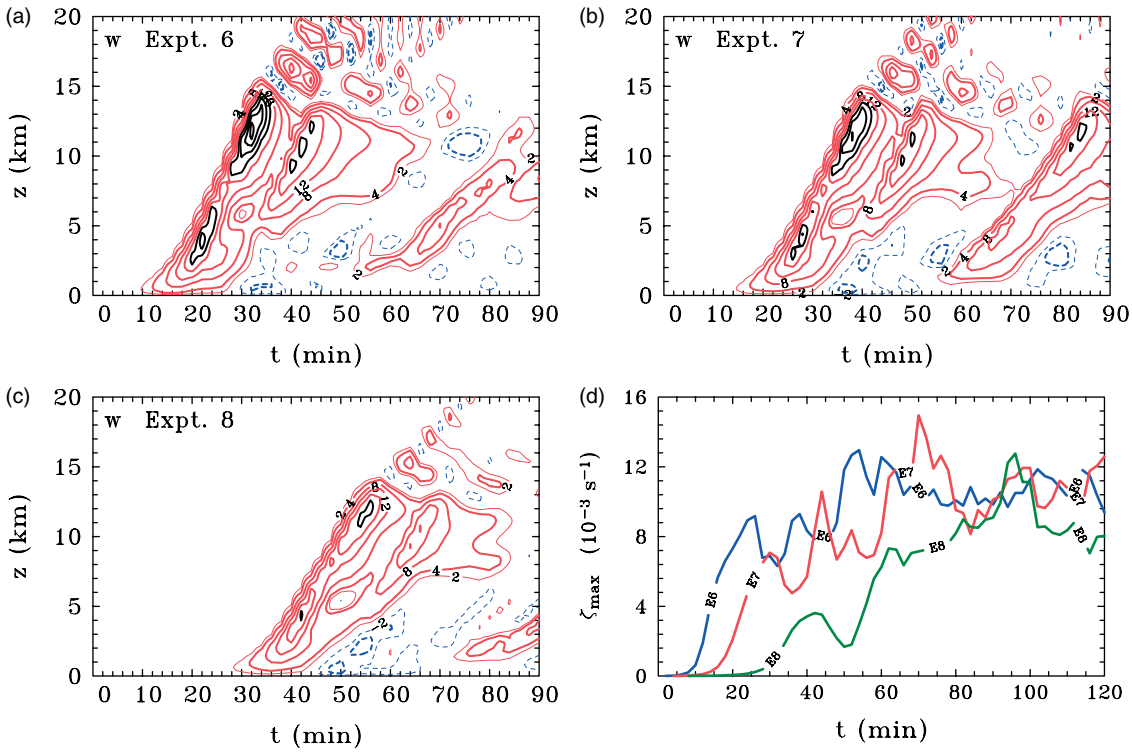

Figure 11. Height–time series of maximum vertical velocity w at the centre of the updraught in Experiments 6–8 (panels (a)–(c), respectively). Contour interval for w: thin contours 2 m s^{-1}, thick contours 4 m s^{-1}. Thick black contours show values above 20 m s^{-1} and are in intervals of 5 m s^{-1}. Solid contours (red in the online article) show positive values, dashed contours (blue in the online article) negative values. Panel (d) shows the time evolution of the domain maximum of ζ in these experiments. This figure is available in colour online at wileyonlinelibrary.com/journal/qj

might speculate that a deeper circulation may be less prone to decay, a possibility that merits further investigation.

Results for a limited number of different environmental soundings showed that the maximum amplification of vorticity increases monotonically with the strength of the thermal perturbation used to initiate the convection. However, the amount of increase depends also on the thermodynamic structure of sounding. Thus, in reality, the amplification of vorticity may depend strongly on the strength of the trigger that initiates the convection, which is generally not known. It depends also on the the low-level thermodynamic structure of sounding. Our current understanding of the way in which the amplification of vertical vorticity by stretching in convective clouds influences tropical cyclogenesis is not yet complete. However, there is mounting evidence that the interaction between the vorticity remnants of clouds promotes an upscale cascade of cyclonic vorticity that is an important component in the formation of a nascent cyclone-scale vortex. This work is conceived as a useful building block for future studies of this issue.

Acknowledgements

We thank Dr Ulrike Wissmeier for the considerable assistance provided in setting up the numerical model and Dr George Bryan for generously making the model available. We are grateful to the Principal Investigator for the PREDICT experiment, Professor Michael Montgomery, for many stimulating discussions about the possible role of deep convection on the dynamics of tropical cyclogenesis and for making it possible for the second author to participate in the experiment. We are grateful also to the PREDICT team for providing quality-controlled data from the experiment. This research was supported by the German Research Council (Deutsche Forschungsgemeinschaft) under Grant No. SM30/25-1.

References

Bolton D. 1980. The computation of equivalent potential temperature. *Mon. Weather Rev.* **108**: 1046–1053.

Braun SA, Montgomery MT, Mallen KJ, Reasor PD. 2010. Simulation and interpretation of the genesis of Tropical Storm *Gert* (2005) as part of the NASA Tropical Cloud Systems and Processes Experiment. *J. Atmos. Sci.* **67**: 999–1025.

Braun SA, Sippel JA, Nolan DS. 2012. The impact of mid-level dry air on hurricane intensity in idealized simulations with no mean flow. *J. Atmos. Sci.* **69**: 236–257.

Brown RG, Zhang C. 1997. Variability of midtropospheric moisture and its effect on cloud-top height distribution during TOGA COARE. *J. Atmos. Sci.* **54**: 2760–2774.

Bryan GH. 2002. '*An investigation of the convective region of numerically simulated squall lines*', PhD thesis, 181pp. Pennsylvania State University.

Bryan GH, Fritsch JM. 2002. A benchmark simulation for moist nonhydrostatic numerical models. *Mon. Weather Rev.* **130**: 2917–2928.

Dunion JP, Veldon CS. 2004. The Impact of the Saharan Air Level on Atlantic Tropical Cyclone Activity. *Bull. Am. Meteorol. Soc.* **85**: 353–365.

Dunkerton TJ, Montgomery MT, Wang Z. 2009. Tropical cyclogenesis in a tropical wave critical layer: easterly waves. *Atmos. Chem. Phys.* **9**: 5587–5646.

Emanuel KA. 1989. The finite amplitude nature of tropical cyclogenesis. *J. Atmos. Sci.* **46**: 3431–3456.

Emanuel KA. 1994. *Atmospheric convection*. Oxford University Press: Oxford; 580pp.

Fang J, Zhang F. 2010. Initial development and genesis of Hurricane Dolly (2008). *J. Atmos. Sci.* **67**: 655–672.

Ferrier BS, Houze RA. 1989. One dimensional time-dependent modelling of GATE cumulonimbus convection. *J. Atmos. Sci.* **46**: 330–352.

Fierro AO, Zipser EJ, Lemone MA, Straka JM, Simpson J. 2012. Tropical oceanic hot towers: need they be dilute to transport energy from the

boundary layer to the upper troposphere effectively? An answer based on trajectory analysis of a simulation of a TOGA COARE convective system. *J. Atmos. Sci.* **69**: 195–213.
Frank WM. 1987. Tropical cyclone formation. In *A Global View of Tropical Cyclones*, Elsberry RL (ed). Office of Naval Research: Washington, DC; pp. 53–90.
Gilmore MS, Straka JM, Rasmussen EN. 2004. Precipitation and evolution sensitivity in simulated deep convective storms: comparisons between liquid-only and simple ice and liquid phase microphysics. *Mon. Weather Rev.* **132**: 1897–1916.
Haynes P, McIntyre ME. 1987. On the evolution of vorticity and potential vorticity in the presence of diabatic heating and frictional or other forces. *J. Atmos. Sci.* **44**: 828–841.
Hendricks EA, Montgomery MT, Davis CA. 2004. On the role of 'vortical' hot towers in formation of tropical cyclone *Diana* (1984). *J. Atmos. Sci.* **61**: 1209–1232.
Holloway CE, Neelin JD. 2009. Moisture vertical structure, column water vapor, and tropical deep convection. *J. Atmos. Sci.* **66**: 1665–1683.
Holton JR. 2004. *An Introduction to Dynamic Meteorology*. Academic Press: London; p 535.
Houze RA, Lee W-C, Bell MM. 2009. Convective contribution to the genesis of hurricane *Ophelia* (2005). *Mon. Weather Rev.* **137**: 2778–2800.
James RP, Markowski PM. 2009. A numerical investigation of the effects of dry air aloft on deep convection. *Mon. Weather Rev.* **138**: 140–161.
Karyampudi VM, Pierce HF. 2002. Synoptic-scale influence of the Saharan air layer on tropical cyclogenesis over the eastern Atlantic. *Mon. Weather Rev.* **130**: 3100–3128.
Kuchera EL, Parker MD. 2006. Severe convective wind environments. *Weather and Forecasting* **21**: 595–612.
LeMone MA, Zipser EJ. 1980. Cumulonimbus vertical velocity events in GATE. Part I: Diameter, intensity and mass flux. *J. Atmos. Sci.* **37**: 2444–2457.
McBride JL. 1995. Tropical cyclone formation. In *Global Perspectives on Tropical Cyclones*, Elsberry RL (ed), WMO/TD-No 693, 289pp. World Meteorological Organization: Geneva; pp. 21–62.
Minoru C, Sugiyama M. 2010. A cumulus parameterization with state-dependent entrainment rate. Part I: Description and sensitivity to temperature and humidity profiles. *J. Atmos. Sci.* **67**: 2171–2193.
Montgomery MT, Smith RK. 2011. 'Tropical cyclone formation: Theory and idealized modelling'. In *Proceedings of Seventh WMO International Workshop on Tropical Cyclones (IWTC-VII), La Réunion, November 2010 (WWRP 2011-1)*. World Meteorological Organization: Geneva, Switzerland.
Montgomery MT, Nicholls ME, Cram TA, Saunders AB. 2006. A vortical hot tower route to tropical cyclogenesis. *J. Atmos. Sci.* **63**: 355–386.
Montgomery MT, Nguyen SV, Smith RK. 2009. Do tropical cyclones intensify by WISHE? *Q. J. R. Meteorol. Soc.* **135**: 1697–1714.
Montgomery MT, Davis C, Dunkerton T, Wang Z, Velden C, Torn R, Majumdar S, Zhang F, Smith RK, Bosart L, Bell MM, Haase JS, Heymsfield A, Jensen J, Campos T, Boothe MA. 2012. The Pre-Depression Investigation of Cloud Systems in the Tropics (PREDICT) Experiment: Scientific basis, new analysis tools, and some first results. *Bull. Am. Meteorol. Soc.* **93**: 153–172.
Nguyen SV, Smith RK, Montgomery MT. 2008. Tropical-cyclone intensification and predictability in three dimensions. *Q. J. R. Meteorol. Soc.* **134**: 563–582.
Ooyama KV. 1969. Numerical simulation of the life cycle of tropical cyclones. *J. Atmos. Sci.* **26**: 3–40.
Redelsperger JL, Parsons DB, Guichard F. 2002. Recovery processes and factors limiting cloud-top height following the arrival of a dry intrusion observed during TOGA COARE. *J. Atmos. Sci.* **59**: 2438–2457.
Rozoff CM. 2007. '*Aspects of moat formation in tropical cyclone eyewall replacement cycles*', PhD thesis, 165pp. Colorado State University.
Saunders AB, Montgomery MT. 2004. *A closer look at vortical hot towers within a tropical cyclogenesis environment*, *Atmospheric Science Bluebook* No. 752. Colorado State University: Fort Collins, CO.
Shin S, Smith RK. 2008. Tropical-cyclone intensification and predictability in a minimal three-dimensional model. *Q. J. R. Meteorol. Soc.* **134**: 1661–1671.
Smith RK, Montgomery MT. 2012. Observations of the convective environment in developing and non-developing tropical disturbances. *Q. J. R. Meteorol. Soc.* DOI: 10.1002/qj.1910.
Sobel AH, Yuter SE, Bretherton CS, Kiladis GN. 2004. Large-scale meteorology and deep convection during TRMM KWAJEX. *Mon. Weather Rev.* **132**: 422–444.
Tompkins AM. 2001. Organization of tropical convection in low vertical wind shears: The role of water vapor. *J. Atmos. Sci.* **58**: 529–545.
Tory K, Frank WM. 2010. Tropical cyclone formation. In *Global perspectives on tropical cyclones: From science to mitigation*. Kepert JD, Chan JCL (eds). *Series on Asia–Pacific Weather and Climate* Vol. 4. World Scientific: Singapore.
Trier SB, Skamarock WC, LeMone MA, Parsons DB, Jorgensen DP. 1996. Structure and evolution of the 22 February 1993 TOGA COARE squall line: numerical simulations. *J. Atmos. Sci.* **53**: 2861–2886.
Weisman ML, Klemp JB. 1982. The dependence of numerically simulated convective storms on vertical wind shear and buoyancy. *Mon. Weather Rev.* **110**: 504–520.
Wissmeier U. 2009. '*The physics of tropical convection*', PhD thesis, 124pp. Ludwig-Maximilians University of Munich: Munich.
Wissmeier U, Smith RK. 2011. Tropical-cyclone convection: the effects of ambient vertical vorticity. *Q. J. R. Meteorol. Soc.* **137**: 845–857.
Wissmeier U, Smith RK, Goler R. 2010. The formation of a multicell thunderstorm behind a sea-breeze front. *Q. J. R. Meteorol. Soc.* **136**: 2176–2188.

